



Facile synthesis of the atomically dispersed hydrotalcite oxide supported copper catalysts for the selective hydrogenation of 5-hydroxymethylfurfural into 2,5-bis(hydroxymethyl)furan



Raju Kumar ^{a,b,c}, Hsin-Hui Lee ^a, En Chen ^a, Yuan-Peng Du ^a, Chan-Yi Lin ^a, Warot Prasanseang ^e, Thanasak Solos ^e, Kittisak Choojun ^e, Tawan Sooknoi ^e, Rui-Kun Xie ^f, Jyh-Fu Lee ^f, Po-Wen Chung ^{a,d,*}

^a Institute of Chemistry, Academia Sinica, 128 Academia Road, Section 2, Nankang, Taipei 11529, Taiwan

^b Department of Applied Chemistry, National Yang Ming Chiao Tung University, 1001 Ta-Hsueh Rd., Hsinchu 30010, Taiwan

^c Sustainable Chemical Science and Technology (SCST), Taiwan International Graduate Program (TIGP), Academia Sinica, Nankang, Taipei 11529, Taiwan

^d Department of Chemistry, National Sun Yat-sen University, Kaohsiung 80424, Taiwan

^e Department of Chemistry, School of Science, King Mongkut's Institute of Technology Ladkrabang, Chalongkrung Road, Ladkrabang, Bangkok 10520, Thailand

^f National Synchrotron Radiation Research Center, Hsinchu 30076, Taiwan

ARTICLE INFO

Keywords:

Atomically dispersed hydrotalcite oxide supported copper catalyst
Selective hydrogenation
5-hydroxymethylfurfural
2
5-bis(hydroxymethyl)furan

ABSTRACT

The selective hydrogenation of 5-hydroxymethylfurfural (HMF) to 2,5-bis(hydroxymethyl)furan (BHMF) using the atomically dispersed supported copper catalyst is investigated. The hydrotalcite oxide supported copper materials ($\text{Cu}_{(x)}\text{HTO}$) are facilely prepared by coprecipitating metal precursors in a methanolic solution under a tuned pH. The surface characterization involving PXRD, TEM, $\text{H}_2/\text{N}_2\text{O}$ -TPR, and XAS reveals unequivocal evidence for the presence of the atomically dispersed copper on HTO surface. XAS specifically indicates the formation of mononuclear copper species, and $\text{H}_2/\text{N}_2\text{O}$ -TPR strongly supports the copper atoms of $\text{Cu}_{(5)}\text{HTO}$ are evenly distributed in 99% dispersion. Moreover, the reduced $\text{Cu}_{(5)}\text{HTO}$ ($r\text{-}\text{Cu}_{(5)}\text{HTO}$) enables to completely hydrogenate HMF to BHMF under mild conditions, in comparison to the poor reactivity catalyzed by the hydrotalcite oxide supported copper nanoparticles ($r\text{-}\text{Cu}_{(4)}@\text{HTO}$). The dramatic enhancement of HMF hydrogenation catalyzed by $r\text{-}\text{Cu}_{(5)}\text{HTO}$ can be attributed to the fine distribution of copper atoms which are situated homogeneously over HTO surface as well as chemically reactive for the carbonyl group.

1. Introduction

To meet the milestone of net-zero carbon emission while maintaining the supply chain of essential chemicals by 2050, the bio-based chemicals derived from renewable feedstocks can serve as a colossal replacement which can mitigate the global commodity consumption derived from petroleum-based chemicals [1,2]. The C6 furanic, 5-hydroxymethylfurfural (HMF), which can be readily produced from lignocellulosic biomass waste, is regarded as one of the most versatile platform molecules [3]. Owing to the different chemical activity of multi-functional groups within the same molecule, HMF can be chemically transformed into a wide spectrum of downstream derivatives, such as 2,5-Bis(hydroxymethyl)tetrahydrofuran (BHMTF), 2,5-dimethylfuran (DMF), 2,5-bis(hydroxymethyl)furan (BHMF), 2,5-furandicarboxylic acid (FDCA) and

others [4–10]. Amid those functional furanics, BHMF through the selective hydrogenation of HMF is of particular interest due to its wide application for polymer production, pharmaceuticals, adhesives, and other fine chemicals [5,8]. However, to hydrogenate HMF to BHMF selectively under mild conditions still necessitates the rational design of the novel catalytic system, which can specifically reduce the carbonyl moiety ($\text{C}=\text{O}$) of HMF [11].

In principle, BHMF can be chemically reduced from HMF by adding stoichiometric equivalence of NaBH_4 , followed by further purification [12]. Recently, the dinuclear Ru-based Shvo's complex can homogeneously catalyze HMF to BHMF in high yield under mild condition [13]. Very lately, the supported Pt-based catalyst can selectively hydrogenate HMF to BHMF under mild conditions, although the major focus was placed on the furfural to furfuryl alcohol [14]. Although a plethora of

* Corresponding author at: Institute of Chemistry, Academia Sinica, 128 Academia Road, Section 2, Nankang, Taipei 11529, Taiwan.

E-mail address: cedricchung@gate.sinica.edu.tw (P.-W. Chung).

heterogeneous catalysts involving noble metals for the selective hydrogenation of carbonyl moiety of HMF to BHMF is extensively reported [11,14–17], the supported Cu-based catalysts are of particular interest thereof [5,6,11]. Apart from being non-precious metal, the prior DFT study suggests that the active Cu metal surface exhibited the strong electronic repulsion between the 3d valence shell of copper atoms and the anti-bonding orbital of the furan ring, which would result in the preferential interaction with the carbonyl moiety of HMF [18]. In addition, the presence of partially oxidized ($\text{Cu}^{1+}/\text{Cu}^{2+}$) copper species on the surface can act as Lewis acid sites to facilitate the adsorption of the carbonyl group via lone-pair electron of oxygen and thus enhance the activity of the C=O group in HMF. Therefore, the supported Cu-based catalysts have been widely explored for selective hydrogenation of HMF to BHMF [5,6,11,15].

Among a myriad of supported Cu-based catalysts, layer double hydroxides (LDHs) is of great potential for the auxiliary materials due to the high tunability, high stability as well as being economically viable [19]. Hence, copper-incorporated LDH materials have reportedly been prepared and employed to catalyze the selective hydrogenation of HMF. Kumalaputri et al. have demonstrated Cu₂₀-PMO (20 mol%) can completely hydrogenate HMF to BHMF up to 99% yield at 100 °C under 50 bar of hydrogen for 3 h, and the selectivity toward DMF was presented as the reaction temperature was elevated at 220 °C [20]. Recently, Wang et al. reported that Cu/MgAlO_x are selectively active in the C=O hydrogenation of HMF to BHMF while Co@Cu/3CoAlO_x can navigate the hydrogenation toward the hydrogenolysis for DMF production at 180 °C under 1.0 MPa of hydrogen [21]. This study revealed that engineering the interface between Cu-nanoparticles and supports by regulating the elemental composition can direct the hydrogenation pathway differently. Notably, the LDH-supported copper nanoparticles were also reported catalytically active for the hydrogenation of furfural to furfuryl alcohol through catalytic transfer hydrogenation in the absence of hydrogen [22–24]. Above all, the effect of the copper metal dispersion on support still remains unclear for the selective hydrogenation of HMF, even though the nature of the support strongly affects the degree of metal dispersion [11].

Recently, the atomically dispersed supported metal catalyst has been regarded as the most intriguing material possessing the advantages for both homogeneous and heterogeneous catalysis, and it has drawn great attention due to the unique structural and electronic properties of the active metals, which could lead to the enormous performance for selective catalysis [25–30]. Herein, we have successfully demonstrated the facile synthesis of the atomically dispersed hydrotalcite oxide supported copper catalysts (Cu_(x)HTO) by simply coprecipitating the metal nitrate precursors altogether in methanolic aqueous solution in a tuned pH instead of the complicated fabrication as previously reported [31–34]. As a result, the copper species on HTO surface after the thermal reduction (r-Cu_(x)HTO) exhibits atomically dispersed features with strong spectroscopic (PXRD, X-ray absorption spectroscopy (XAS)) and microscopic (TEM) supports. Among those aforementioned analysis, the absence of metal-metal shells (2nd shell) in the extended X-ray absorption fine structure spectra (EXAFS) manifests the presence of mononuclear copper species on HTO. Moreover, the temperature-programmed chemical redox analysis (H₂/N₂O/H₂-TPR) substantiates that the copper species are highly dispersed to a degree of at least 97% over the HTO surface, even though the copper doping is increased to 20 mol%. Notably, the selective hydrogenation of HMF catalyzed by the r-Cu₍₅₎HTO was carried out at 125 °C under 5 bar of H₂ for 1 h, and the catalytic performance shows that the r-Cu₍₅₎HTO can completely hydrogenate HMF and selectively transform HMF into BHMF with nearly 100% yield. In contrast, the r-Cu₍₄₎@HTO catalyst, which was simply prepared by the impregnation method, presents poor reactivity of the hydrogenation of HMF, and it could be attributed to the poor copper dispersion on HTO surface.

2. Experimental section

2.1. Materials

Cu(NO₃)₂·3 H₂O (Sigma-Aldrich, 99.9%), Mg(NO₃)₂·6 H₂O (Alfa-Aesar, 98–102%), Al(NO₃)₃·9 H₂O (Fisher Scientific, 98%), Na₂CO₃ (Sigma-Aldrich, 99.8%), NaOH (Shimakyu's Pure Chemicals, 99.4%), methanol (Macron fine chemicals, ≥99.8%) and isopropanol (IPA) (Fisher Scientific, 99.8%), HMF (AK Scientific, 98%), BHMF (Combi Blocks, 97%) chemicals were purchased and used without further purification. Deionized (DI) water was used for all purposes.

2.2. Preparation of hydrotalcite-derived supported copper (Cu_(x)HTO) catalysts

The hydrotalcite (HT) supported copper catalysts were prepared by coprecipitation of metal nitrate precursors in methanolic solution (V_{methanol}/V_{water} = 1:1) at tuned pH. For the preparation of Cu_(x)HTO, the copper precursor was added stoichiometrically in a formula of Cu_(x)Mg_(75-x)Al₍₂₅₎O, where x represents mol% of copper within the structure. Typically, Cu(NO₃)₂·3 H₂O (0.322 g), Mg(NO₃)₂·6 H₂O (4.788 g), and Al(NO₃)₃·9 H₂O (2.5 g) were dissolved in 200 mL of methanolic solution for the preparation of 5 mol% of copper doping. The nitrate mixture was added dropwise into the beaker containing 200 mL methanolic solution at a rate of 2 mL/min under vigorous magnetic stirring at room temperature. The pH of the mixture solution was maintained at 10 ± 0.3 by adding an alkaline solution prepared by mixing Na₂CO₃ (0.0142 g/mL) and NaOH (0.0177 g/mL) in methanolic solution. After the complete addition, the suspension was further stirred at the same pH for another 10 min. The pale blue slurry was transferred into a 1 L high-density polyethylene (HDPE) bottle and sealed for static aging at 65 °C for 24 h under ambient pressure. After aging, the solid was filtered and washed with DI water until the filtrate reached neutral pH. The resultant solid denoted Cu₍₅₎HT was dried at 90 °C for 24 h prior to the thermal treatment. The Cu₍₅₎HTO material was obtained by calcining the Cu₍₅₎HT at 550 °C for 12 h with a heating ramp rate of 2 °C/min under the airflow (40 mL/min). Pristine hydrotalcite oxide (HTO) was prepared by the same synthesis protocol. Prior to the catalytic test, all copper-based catalysts were reduced at 350 °C for 4 h under the H₂ gas flow (100 mL/min) and denoted as r-Cu_(x)HTO.

2.3. Preparation of copper-loaded hydrotalcite oxide (Cu₍₄₎@HTO) catalyst

The copper-loaded hydrotalcite oxide (Cu₍₄₎@HTO) catalyst with a copper loading of 5 wt% was prepared by the wet-impregnation method. First, Cu(NO₃)₂·3 H₂O (0.095 g) was dissolved in 3 mL of ethanol, and the solution was added dropwise in HTO (0.5 g) by precisely mixing to form a homogeneous pale blue solid paste, which was placed for drying at 90 °C for 12 h. The Cu₍₄₎@HTO was reduced by the aforementioned conditions, and the resultant sample was denoted as r-Cu₍₄₎@HTO.

2.4. Catalyst characterization

The elemental analysis was carried out using an inductively coupled plasma optical emission spectrometer (ICP-OES, Agilent 725, USA). Before analysis, 50 mg of catalyst was completely dissolved in the mixture of 4 mL of aqua regia and 0.4 mL of hydrofluoric acid. After complete dissolution, 50 mL of H₂O was added and further diluted 30 times and then injected for analysis.

The structure and crystallinity of prepared materials were measured by powder X-ray diffraction (PXRD, Bruker D8 Advance, Germany) instrument, and the X-ray diffractometer using Cu K α radiation ($\lambda = 1.5406 \text{ \AA}$) was operated at a voltage (40 kV) and current (40 mA). All diffraction patterns were accumulated in a scan range from 5° to 90° with a 20 steps rate was 0.5 s per step through a 0.6 mm wide Cu slit. The

spectra were smoothed and baseline corrected after measurement using EVA software. The crystallite size of the material was also estimated using the Scherrer equation through EVA software.

The texture of prepared catalysts was measured using N₂ sorption isotherm on a 3-Flex surface analyzer (Micromeritics, USA) equipment. The N₂ physisorption experiment was conducted under liquid N₂ (77 K), and the surface area was estimated by using Brunauer-Emmett-Teller (BET) equation. Prior to the measurement, 70 mg of the sample was pretreated at 350 °C in a vacuum for 12 h.

The morphology of the samples was measured by high-resolution transmission electron microscopy (HR-TEM, JEM-2100 F, JEOL, Japan), and the system was operated at 200 kV. High-angle annular dark-field scanning transmission electron microscopy (HAADF-STEM) images and energy-dispersive X-ray spectroscopy (EDX) mapping images were collected for copper particles and their dispersion in the samples. Before the TEM measurement, 1 mg of catalyst powder was suspended in one mL of ethanol by sonication. A drop of the resulting suspension was then dispersed onto the commercially available carbon-lacey nickel grid (300 mesh) and dried at ambient temperature.

The copper dispersion and metallic copper surface area of prepared catalysts were determined by dissociative N₂O adsorption and subsequent H₂-TPR technique by a self-designed H₂/N₂O-TPR system equipped with a thermal conductivity detector (TCD, VICI). Prior to the reduction process, 15 mg of the catalyst was pretreated in the air at 400 °C (10 °C/min) for 2 h and cooled down to 50 °C under the N₂ atmosphere. For the first H₂-TPR (1st H₂-TPR), the catalyst was reduced under 10% H₂/Ar mixture from 50° to 350°C (heating rate 10 °C/min) and held at 350 °C for 2 h. Subsequently, the reduced sample was cooled down to 60 °C under an N₂ atmosphere and then exposed to a pure N₂O stream (30 mL/min) at 60 °C for 1 h to ensure complete oxidation of surface metallic copper. Further, N₂O was flushed with N₂ (30 mL/min) at 60 °C for 0.5 h and then raised the temperature to 110 °C and held for 0.5 h to flush out the excess absorbed N₂O. To quantify the surface copper species, the oxidized copper species underwent for second H₂-TPR (2nd H₂-TPR) process, which was executed from room temperature to 350 °C. The H₂ consumption from both H₂-TPR was monitored with TCD. The copper dispersion (D_{Cu}) was estimated by the fraction of hydrogen consumption by copper (2nd H₂-TPR) over total hydrogen consumption by copper (1st H₂-TPR). Moreover, the copper dispersion, and specific surface area of metallic copper were calculated, as described elsewhere [35].

X-ray absorption spectroscopy (XAS) spectra at the Cu K-edge were obtained using synchrotron radiation in transmission mode at the beamline TLS-17C1 of the National Synchrotron Radiation Research Center (NSRRC), Taiwan. The light source provided photon energy ranging from 4 keV to 15 keV, and the incident X-ray was monochromatized by a Si(111) double-crystal monochromator. The Cu K-edge XAS spectra were recorded in a transmission mode with the intensity of incident and transmitted X-ray beams measured by gas-filled ionization chambers, and Cu-foil, Cu₂O, and CuO were used as standards. In addition, the real-time X-ray absorption near-edge structure (XANES) spectra at Cu K-edge were carried out in a compact in-situ cell system equipped with the temperature-programmed reduction under H₂ gas (50 mL/min) flow. All recorded raw data were processed using the Athena and Artemis software version 0.9.26, including the Demeter package [36].

High-resolution electrospray ionization (HR-ESI) mass spectrometry was employed to validate the BHMF derived from HMF hydrogenation using the commercial BHMF as a reference. The measurement was conducted on a double-focusing mass spectrometer (JMS-700, JEOL, Japan) with a resolution of 8000.

The ¹H and ¹³C Nuclear Magnetic Resonance (NMR) spectrometer (Advance V-500 M, Bruker, Germany) measurements were used to identify the BHMF derived from HMF hydrogenation using the commercial BHMF as reference. The ¹H and ¹³C NMR spectra were collected using D-methanol solvent.

2.5. Catalytic test

The catalytic hydrogenation reaction of HMF into BHMF was performed using the Biotage Endeavor Catalyst Screening System. Prior to the catalytic reaction, the catalyst was thermally reduced in the presence of hydrogen at 350 °C for 4 h. In the typical reaction experiment, 10 mg ± 0.2 of catalyst and 4 mL of 20 mM HMF (in IPA) solution were transferred into a glass liner which was placed into the reactor system (14 mL) and sealed. After that, the catalytic reaction was carried on at the optimized reaction conditions, with a constant stirring rate of 400 rpm. Once the reaction was completed, the reactor was allowed to cool down naturally at room temperature. Then, the supernatant was withdrawn, filtered, and the filtrate was used for analysis. The HMF and derived products such as BHMF, 5-Methylfurfural (5-MF), 5-Methyl-2-furan methanol (MFA), DMF, Furfuryl alcohol (FUL), BHMTHF and 2,5-Dimethyltetrahydrofuran (DMTHF) were analyzed using a gas chromatograph (GC-2014, Shimadzu, Japan) equipped with a flame ionization detector (FID) and 60-meter capillary column (SH-RXI 5MS, Shimadzu). The external calibration method was used to quantify the HMF and its derived products in the reaction mixture, and the individual calibration curves of standards are presented in Fig. S1. In addition, ¹H NMR, ¹³C NMR, and Mass-spectra characterization techniques were used to confirm the BHMF structure after reaction, in comparison with standard BHMF thereof, and the results are presented in Fig. S2a-c. The HMF conversion, the yield of the catalyzed products, and the carbon balance were estimated by using the following equations:

$$\text{HMF conversion}(\%) = \left(1 - \frac{\text{Moles of HMF in products}}{\text{Starting moles of HMF}} \right) \times 100\%$$

$$\text{Product yield}(\%) = \frac{\text{Moles of products (e.g. BHMF)}}{\text{Starting moles of HMF}} \times 100\%$$

$$\text{Carbon balance}(\%) = \frac{\text{Total carbon mole content of each product}}{\text{Moles of carbon in converted HMF}} \times 100\%$$

All the experiments were triplicated, and the carbon balance was calculated to be ~100. For the recyclability study, the spent catalyst was recovered from the reaction mixture after the reaction through filtration and washed with IPA to remove the organic adsorbents, followed by drying at 50 °C overnight. The resultant spent catalyst was thermally reduced at 350 °C for 3 h under the H₂ gas flow (100 mL/min) prior to the next use.

3. Results and discussions

3.1. Physicochemical characterization

The copper content incorporated in the hydrotalcite (HT) structure through one-pot synthesis was determined by ICP-OES, and the resulting materials were denoted as r-Cu_(x)HTO, where x represents the molar percentage of copper. As shown in Table S1, an agreement was practically found in copper quantity between the ICP-OES results and the introductory amounts. It suggests that we could readily substitute Cu²⁺ for Mg²⁺ within Cu_(x)HT by precisely adding Cu²⁺_(aq) during the coprecipitation. In addition, the bluish-green Cu_(x)HT reveals that Cu²⁺ has been apparently incorporated into HT structure.

PXRD measurements can render diffraction patterns of the crystalline structure of materials. Fig. 1a presents that the as-synthesized HT as well as Cu_(x)HT materials with various degrees of copper doping exhibit well-resolved peaks of the characteristic crystalline phase of layer double hydroxide (JCPDS No. 14-0191) [37–39]. Unlike the CuO-tremolite phase observed in the previous study [40], no traceable formation of other copper species is observed for Cu₍₁₀₎HT, which possesses the significantly high copper doping thereof. It can be inferred that copper cations can partially replace the magnesium cations, which

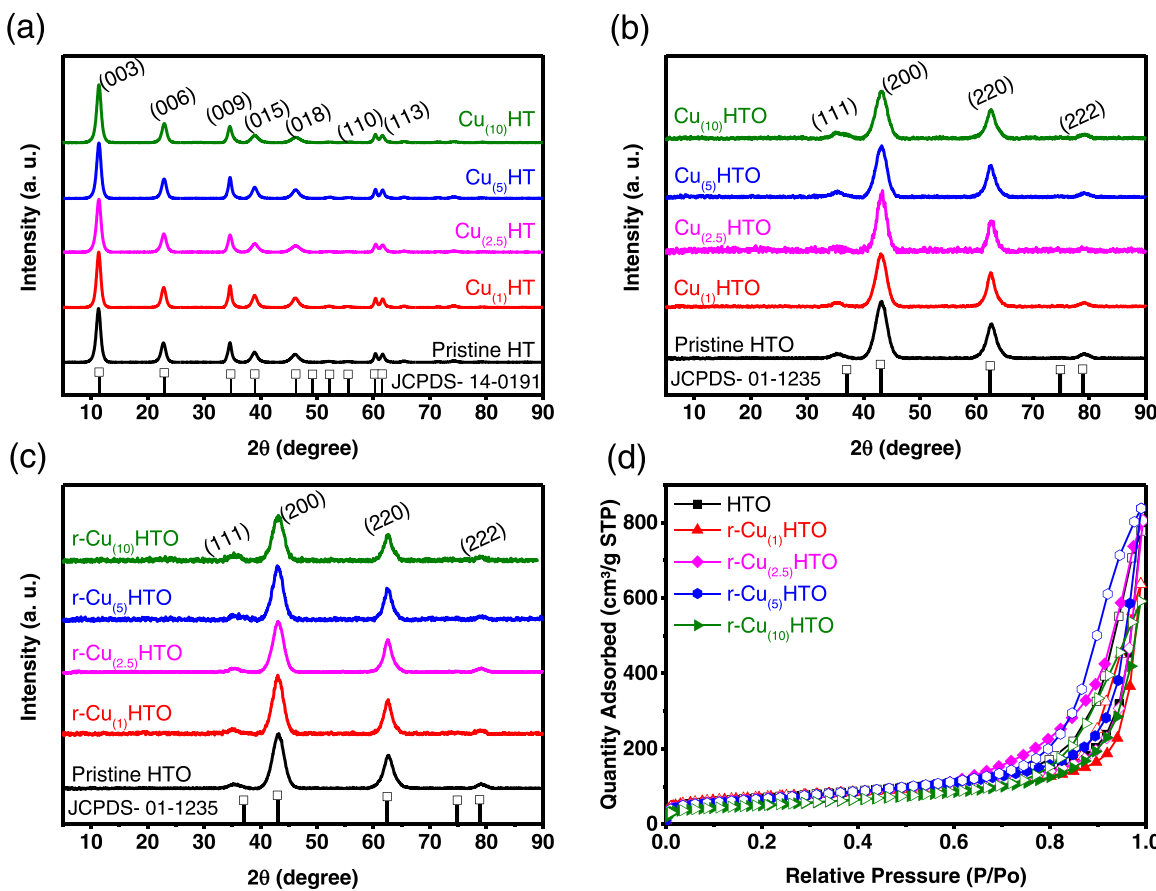


Fig. 1. PXRD patterns of (a) as-synthesized HT and Cu_(x)HT, (b) calcined HTO and Cu_(x)HTO, (c) reduced r-Cu_(x)HTO, (d) N₂ sorption isotherms of HTO and r-Cu_(x)HTO samples.

results in being structurally situated in the center of the octahedral union for the brucite layer of LDH structure [41].

Copper-doped hydrotalcite-derived oxide denoted Cu_(x)HTO was simply synthesized by calcination of Cu_(x)HT at 550 °C. The calcination process encompassing dehydration, decarbonization as well as dehydroxylation of the interlayers of LDH materials could easily transform a 2D brucite-like HT into a 3D cubic-like HTO [42], as the diffraction patterns illustrated in Fig. 1b. Both Cu_(x)HTO and the pristine HTO present well-resolved peaks at the 35.2°, 43.1°, 62.4°, and 79.1°, which are characteristically indexed to the (111), (200), (220), and (222) diffraction planes of an MgO periclase structure, respectively (JCPDS No. 01-1235) [38]. Noted that neither CuO phase nor alumina structures had been observed, and it indicates that Cu²⁺ replacement can homogeneously incorporate into the framework of Cu_(x)HTO [43].

Moreover, Fig. 1c displays the PXRD diffraction patterns of the reduced copper-doped hydrotalcite oxide denoted as r-Cu_(x)HTO, which has been thermally reduced under the H₂ gas flow at 350 °C. Notably, the resulting r-Cu_(x)HTO materials also exhibit the periclase phase of MgO, resembling the diffraction pattern of parenting materials. Neither metallic copper nor copper oxide peaks are observed conspicuously, even after the consecutive thermal reduction. It can be inferred that the copper replacement of r-Cu_(x)HTO is structurally situated well within the framework. Thus, the highly dispersed copper species over the r-Cu_(x)HTO surface can be expected.

In contrast to copper-doped HTO, the copper-loaded HTO material denoted Cu₍₄₎@HTO was simply prepared by the wet-impregnation process, followed by the same courses of thermal reduction. As shown in Fig. S3a, the material of r-Cu₍₄₎@HTO presents the PXRD pattern as a sum of the scattering from both the periclase MgO phase of HTO and metallic copper. This observation suggests that the impregnation of

copper precursor on HTO support might sporadically form the domains, which leads to form the agglomeration of copper metallic particles after the thermal reduction. Thus, the result substantiates that the coprecipitation method to prepare Cu_(x)HTO materials can disperse the copper domains homogeneously over the framework of HTO, concomitant with no distinct aggregation of copper replacement even after the consecutive thermal reduction.

Nitrogen physisorption measurements were performed to understand the surface texture of solid materials. Fig. 1d illustrates the nitrogen sorption isotherms of pristine HTO and r-Cu_(x)HTO materials, and they all exhibit Type II isotherm looped with H3 hysteresis. This result suggests that r-Cu_(x)HTO might possess plate-like aggregates comprising possible macroporosity contributed from the interspace of the hierarchical interconnection of the layer building blocks of HT after thermal treatment [44]. The BET surface areas (S_{BET}) of r-Cu_(x)HTO materials, as summarized in Table S1, are comparable (215–241 m²/g), although r-Cu₍₅₎HTO exhibits the largest total pore volume (0.67 cm³/g) and the highest external surface area (217 m²/g). In addition, the copper substituents appear to be structurally situated well within the layer HT framework during the facile synthesis of Cu_(x)HT, regardless the degree of copper loadings. Thus, the sequential thermal treatments hardly influence the surface textures of r-Cu_(x)HTO. On the other hand, r-Cu₍₄₎@HTO material which was prepared through the wet-impregnation of copper precursor on HTO, presents a perceptible decrease in the surface area (192 m²/g). It could be attributed to the agglomeration of copper particles obstructing the interspace over the HTO surface after the thermal reduction.

TEM was employed to characterize the morphological and structural properties of solid materials, and the corresponding micrographs are shown in Fig. 2. As the bright-field TEM micrographs present in Figs. 2a

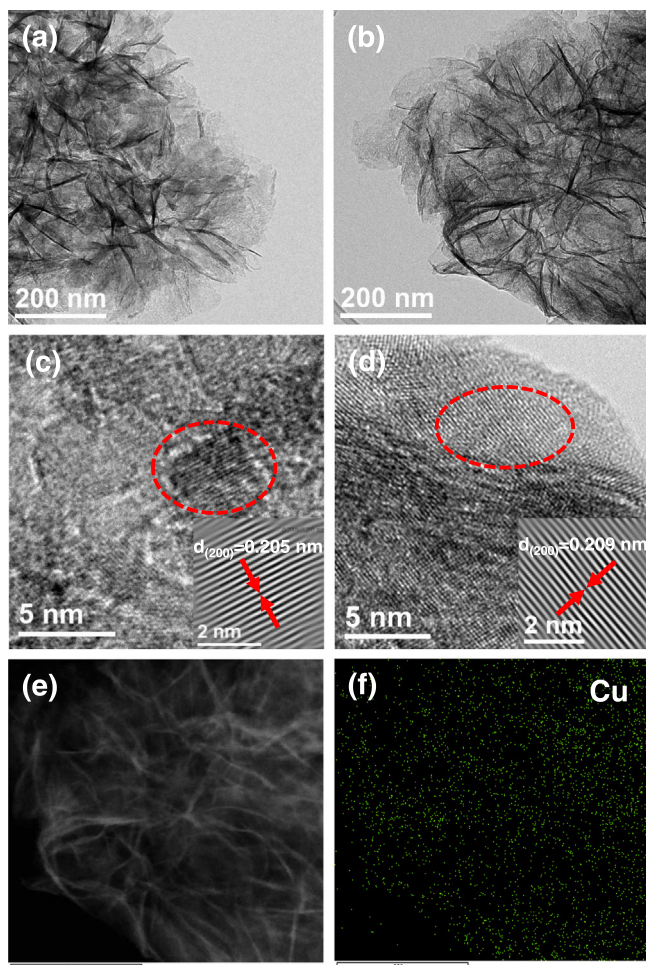


Fig. 2. TEM micrographs of (a) HTO, (b) r-Cu₍₅₎HTO, the *d*-spacings of the (200) plane under high magnification of (c) HTO, (d) r-Cu₍₅₎HTO, HAADF-STEM micrograph of (e) r-Cu₍₅₎HTO and (f) with Cu elemental mapping.

and 2b, r-Cu₍₅₎HTO closely resembles the pristine HTO in leaf-like appearance. This nano-sheet morphology is in good accordance with the surface texture derived from nitrogen physisorption. In addition, TEM micrographs at higher magnifications, shown in Figs. 2c and 2d, clearly reveal the crystalline lattice of both pristine HTO and r-Cu₍₅₎HTO. In view of the above, *d*₍₂₀₀₎ of HTO deduced from TEM micrographs as depicted in the insets exhibits comparably ca. 0.2 nm, which coincides well with the ones derived from PXRD as listed in Table S2. It is noteworthy that no obvious copper metallic particle is observed as darker dots in contrast to the main subject of r-Cu₍₅₎HTO under the bright-field TEM mode. This precedent indicates that the copper substituents, which hardly change the crystalline lattice of HTO might be uniformly distributed within the framework during the synthesis.

To deeply understand the copper distribution over the HTO surface, Figs. 2e and 2f present the HAADF-STEM micrograph of r-Cu₍₅₎HTO and the one with copper elemental analysis by EDX, respectively. Under the dark-field mode, no shining dots on r-Cu₍₅₎HTO is conspicuously discovered as plausible copper agglomeration, which in turn is profoundly detected on r-Cu₍₄₎@HTO as demonstrated in Fig. S3b and S3c. Both bright-field and dark-field TEM micrographs of r-Cu₍₅₎HTO substantiate the homogeneous dispersion of copper replacement on HTO while coprecipitating the metal precursors altogether. TEM image of r-Cu₍₅₎HTO with copper elemental mapping through EDX also corroborates that the copper elements indeed are highly dispersed within the structure of HTO. This homogeneous dispersion suggests the formation

of a solid solution between Cu and HTO, which indicates that copper substituents incorporated into the lattice as previously reported [45], is in good accordance with the PXRD analysis.

To understand the nature of copper dispersion over HTO, a series of chemical temperature-programmed reductions (H₂/N₂O/H₂-TPR) were employed in scrutinizing the reduction temperature of copper and the interaction there within. Table 1 presents the specific surface area of copper (S_{Cu}), and degrees of copper dispersion (D_{Cu}) derived from H₂-TPR profiles, which correspond to the hydrogen consumption as a function of reduction temperature, as depicted in Fig. S4a-c. Both Cu₍₅₎HTO and r-Cu₍₅₎HTO present one major reduction temperature, while Cu₍₄₎@HTO exhibits two distinct reduction regions, as shown in solid lines for the first H₂-TPR. The broad peak centered at 330 °C for Cu₍₄₎@HTO is closely attributed to the reduction of copper oxide nanoparticles in larger sizes on HTO support, which coincides well with the XRD and TEM micrograph for r-Cu₍₄₎@HTO as shown in Fig. S3a-c. The peak reduction temperature centered at 261 °C in conjunction with a broadening tail on Cu₍₅₎HTO indicates the presence of finely dispersed Cu²⁺ species as previously reported [46].

In addition, the strong interaction between copper species and the coordinated oxygens within HTO framework might contribute to the tailing beyond the peak reduction signal [35,47]. The endpoint of the drag on the reduction temperature at 350 °C suggests the utter temperature to completely reduce Cu₍₅₎HTO prior to the catalytic reaction. On the other hand, a similar reduction response is observed for r-Cu₍₅₎HTO, albeit the lower peak reduction temperature at 236 °C. The resemblance between TPR profiles suggests that copper species are distributed in a similar mechanism over the HTO surface, however, the lower peak reduction temperature of r-Cu₍₅₎HTO indicates that the chemical surrounding of copper is likely to be reduced after the thermal reduction under hydrogen. Hence, the reduction process could play a role to restructure the chemical environment of the HTO supported copper atomically, which might lead to the high chemical accessibility for the catalytic reaction.

The NH₃/CO₂ temperature-programmed desorption (TPD) measurement can quantitatively unveil the acid and base sites on the surface among catalysts, and the acid/base sites per surface coverage are summarized in Table S3. The basic coverage of r-Cu₍₅₎HTO is significantly low among those representative catalysts, and it could be attributed to that the atomically dispersed copper species are highly coordinated with neighboring oxygens, concomitant with the decrease of surface hydroxyl groups during the material preparation. In addition, the thermal reduction of Cu₍₅₎HTO results in the acid-base redistribution, and the base coverage is significantly reduced nearly 40% on r-Cu₍₅₎HTO surface. It supports that the thermal reduction could restructure the chemical environment of r-Cu₍₅₎HTO, which is in line with the treatment-induced restructuring as previously reported [48]. For the Cu₍₄₎@HTO material, the narrow distributed reduction peak centered at a lower temperature region at 205 °C on Cu₍₄₎@HTO is also observed because the partial formation of finely dispersed copper sites cannot be completely ruled out, as in a solid solution during the material preparation [49,50]. On the other hand, the formation of sporadic CuO

Table 1
Compositional, textural, and chemical analysis of materials.

Catalyst	Metal Content	N ₂ -sorption	H ₂ /N ₂ O-TPR
	Cu-content ^a (mol%)	S _{BET} ^b (m ² /g)	S _{Cu} ^c (m ² /g _{Cu})
Cu ₍₅₎ HTO	5.1	232	674.5
r-Cu ₍₅₎ HTO	5.1	232	669.2
Cu ₍₄₎ @HTO	4.0	192	449.7
			99.2
			98.7
			66.4

^aElemental composition determined by ICP-OES; ^bSurface area determined by N₂ sorption; ^cThe specific surface area of metallic copper (S_{Cu}) was estimated by the second H₂-TPR profile after N₂O oxidation [35]; ^dThe copper dispersion (D_{Cu}) was estimated by $(2 \times A_2/A_1) \times 100\%$ (A₂ is the second H₂-TPR peak area and A₁ is the first H₂-TPR peak area).

particle sizes on Cu₍₄₎@HTO might result in one broad reduction peak from 250 °C onward as the reported broad responses in H₂-TPR for the silica-supported copper materials beyond 200 °C [51].

To estimate the degree of copper dispersion (D_{Cu}) on surface, the dissociative N₂O adsorption followed by the subsequent H₂-TPR was employed. As presented in dotted lines for the second H₂-TPR in Fig. S4a-c, the surface exposed copper atoms which are specifically oxidized by N₂O, can be reduced at a relatively lower temperature under hydrogen flow. Thereby, D_{Cu} deduced from the integrated areas of 1st and 2nd H₂-TPR profiles exhibit ca. 99% for both Cu₍₅₎HTO and r-Cu₍₅₎HTO catalysts. The results indicate that the copper species are nearly atomically dispersed over HTO supports. The specific surface areas of copper (S_{Cu}) for Cu₍₅₎HTO and r-Cu₍₅₎HTO are higher than 665 m²/g_{Cu}, given the 5 mol% copper amount. It is 2.9-fold higher than the surface area (S_{BET}) of the copper-doped HTO. In other words, the

copper-doped HTO could provide abundant and active mononuclear copper sites on the surface for selective catalysis. On the contrary, the agglomeration of copper oxide particles for Cu₍₄₎@HTO during the preparation leads to lower D_{Cu} (66%) as well as lower S_{Cu} (450 m²/g_{Cu}). Furthermore, it is noteworthy that the degree of copper dispersion for Cu_(x)HTO appears not to be influenced while the molar amount of doping copper (x) is elevated to 20% during the material synthesis. All D_{Cu} for Cu_(2.5-20)HTO maintain greater than 97%, as presented in Fig. S4d, and it concludes that our preparation can render a feasible protocol to synthesize the atomically dispersed supported copper materials.

To understand the detailed electronic and geometric information of copper core on HTO, XAS measurement was employed. Both XANES and EXAFS spectra are presented in Fig. 3. The XANES spectra for both Cu₍₅₎HTO and r-Cu₍₅₎HTO exhibit similar features in the pre-edge

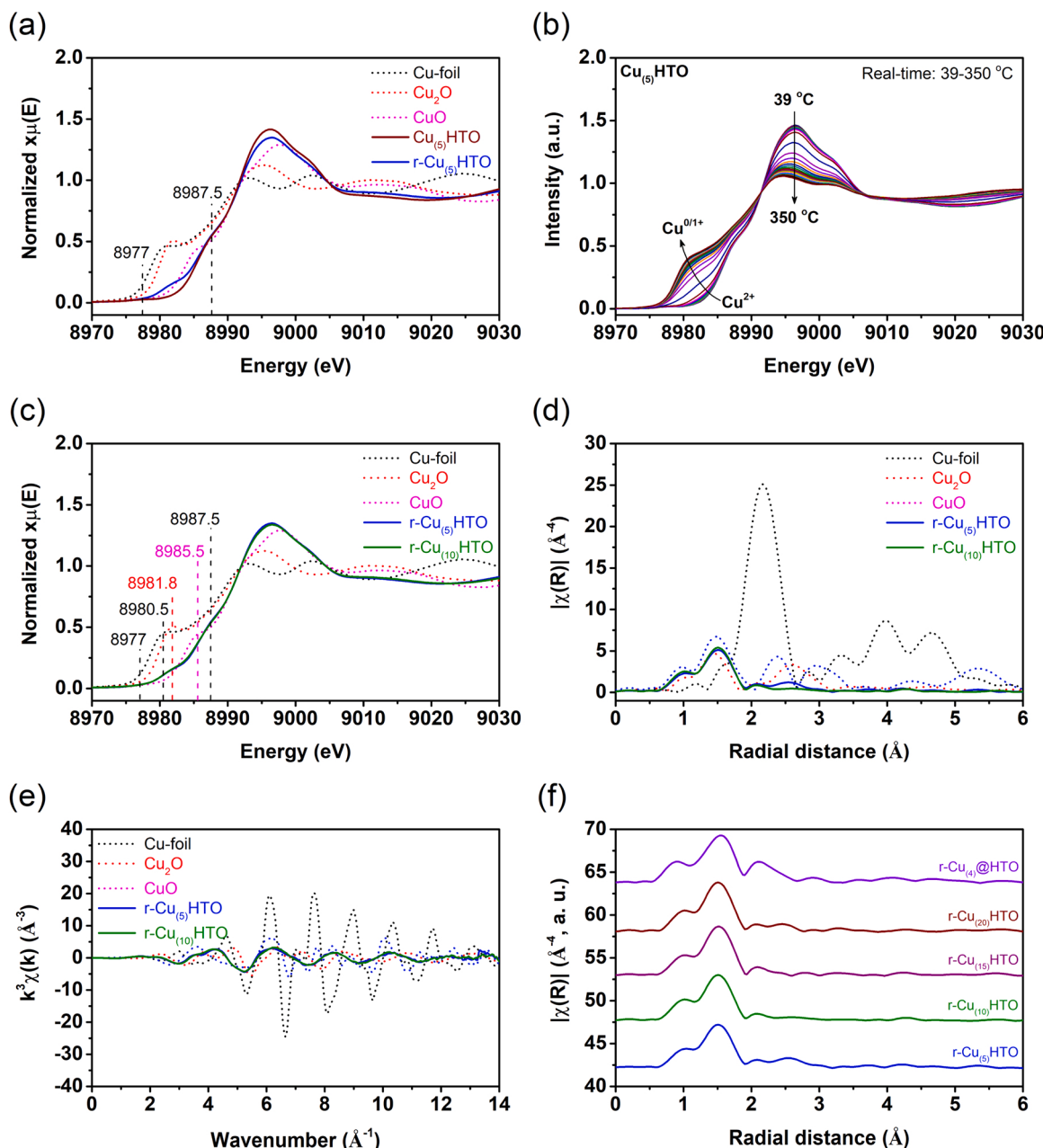


Fig. 3. (a) XANES spectra of Cu-foil, Cu₂O, CuO, Cu₍₅₎HTO and r-Cu₍₅₎HTO, (b) the real-time XANES spectra of Cu₍₅₎HTO catalyst recorded during the hydrogen reduction in the temperature range between 39 and 350 °C, (c) XANES, (d) R-space (no phase correction), (e) K-space of Cu-foil, CuO, Cu₂O, r-Cu₍₅₎HTO and r-Cu₍₁₀₎HTO, (f) R-space (no phase correction) of r-Cu₍₅₋₂₀₎HTO and r-Cu₍₄₎@HTO materials.

region, as shown in Fig. 3a. They share a weak peak located at 8977 eV and a shoulder peak centered at 8987.5 eV, respectively. The traceable peak at 8977 eV, referring to the $1\text{s} \rightarrow 3\text{d}$ transition, is regarded as a fingerprint of Cu^{2+} species [45]. On the other hand, the shift of the shoulder peak at 8987.5 eV in comparison to the CuO standard at 8985 eV is observed. This shoulder peak usually corresponds to $1\text{s} \rightarrow 4\text{p}$ transition, and thereby, the shift is highly affected by the neighboring coordination geometry. It might be attributed to that Cu species are situated in an octahedral or distorted octahedral geometry coordinated by oxygens after replacing Mg occupancy within HT lattice sites [45,52]. A broad shoulder peak ranging between 8979 and 8984 eV in the pre-edge region is also observed in the XANES spectrum of r- $\text{Cu}_{(5)}\text{HTO}$ material. This shoulder peak typically indicates the formation of the non-metallic electronic structure of $\text{Cu}^{\delta+}$ ($0 < \delta < 2$) [53]. It is in accordance with the linear combination fitting (LCF) analysis derived from XANES of r- $\text{Cu}_{(5)}\text{HTO}$ as shown in Fig. S5, and this result suggests that Cu species might not be completely reduced in the presence of hydrogen under the thermal reduction at 350 °C.

To study the chemical change of copper cores on HTO surface during the reduction treatment, the real-time XANES measurement at Cu K-edge was recorded in conjunction with the temperature-programmed reduction under hydrogen. As shown in Fig. 3b, the real-time XANES spectra of the $\text{Cu}_{(5)}\text{HTO}$ in representative sets reveal that the intensity of the white line peak at 8997 eV monotonically diminishes while elevating the reduction temperature. It evolves into a weak doublet, splitting two peaks at 8995 eV and 9002 eV, which indicates the formation of metallic copper. Meanwhile, the shoulder peak at 8982 eV corresponding to metallic copper emerges whilst the temperature increases, and the intensity culminates at the peak temperature of around 350 °C. Therefore, the progressive transformation among the absorption profiles indeed proves that the complete reduction of Cu^{2+} within $\text{Cu}_{(5)}\text{HTO}$ takes place during the thermal reduction under the hydrogen.

Moreover, it is noteworthy that the oxidation state of copper on r- $\text{Cu}_{(5)}\text{HTO}$ unusually increases from Cu^0 to Cu^+ in the presence of hydrogen flow under the same gas-tight environment while cooling down after the reduction at 350 °C, as shown in Fig. S6. The surface copper atoms appear to oxidize and structurally transform to Cu_2O , as the EXAFS fitting suggests. Although the cause of the metallic copper oxidation under hydrogen flow remains unclear, some speculations are listed below: (1) the neighboring oxygen atoms on the hydroxylate oxide surface might immediately coordinate with those copper atoms back to Cu_2O to minimize the surface tension of being transient mononuclearity, (2) the disproportionation of copper might occur if there is a trace of unreduced Cu^{2+} species on the surface, or (3) the plausible surface coordinated molecular copper hydrides might form during the cooling under the hydrogen flow.

On the other hand, Cu^{2+} species is evidently observed on the HTO surface while the r- $\text{Cu}_{(5)}\text{HTO}$ sample was removed from the gas-tight cell after cooling and then purposefully placed in the air for 7 h, as shown in Fig. S7. Therefore, the metallic Cu cores after reduction might be instantly oxidized once the r- $\text{Cu}_{(5)}\text{HTO}$ surface is exposed to the ambient as a trade-off for the high chemical accessibility of copper species. As a result, r- $\text{Cu}_{(5)}\text{HTO}$ predominately consists of the copper species in the form of Cu^{2+} yet some partially reduced $\text{Cu}^{\delta+}$ ($0 < \delta < 2$), which is in accordance with the aforementioned TPR analysis as well as the LCF results. It is also noteworthy that the XANES spectrum of the r- $\text{Cu}_{(10)}\text{HTO}$, which possesses 2-fold of Cu loading, strongly resembles that of the r- $\text{Cu}_{(5)}\text{HTO}$, as shown in Fig. 3c. It indicates that the electronic structures of Cu on HTO are hardly affected despite the higher loading of Cu presented during the synthesis.

As depicted in Figs. 3d and 3e, the EXAFS spectra were demonstrated in sets for both R-space and K-space to elucidate the coordination environment of copper cores on the r- $\text{Cu}_{(5)}\text{HTO}$ surface. Unlike the well-resolved multiple peaks amid the copper-associated standards, the R-space of the r- $\text{Cu}_{(5)}\text{HTO}$ presents one pronounced peak at 1.5 Å (no phase correction), referring to the Cu-O contribution in the first shell.

This observation corroborates that the coordinated oxygen atoms surround the copper cores as the nearest neighboring atoms. Surprisingly, no perceptible peak beyond 2.0 Å corresponding to Cu-Cu contribution is observed, and it indicates that no Cu atoms occupy the second shell, which is evidently presented in Cu_2O or CuO standards. In general, the absence of metal-metal shells (2nd shell) in the EXAFS spectra manifests the presence of mononuclearity for metal species on supports [26]. Therefore, the result unravels that the Cu species can be situated as isolated sites in an upmost atomically dispersed manner on r- $\text{Cu}_{(5)}\text{HTO}$ surface when complemented with the copper dispersion in 99% by the previous TPR study. Moreover, judging from the EXAFS spectra as shown in Fig. 3f, the copper cores remain the mononuclear sites on r- $\text{Cu}_{(x)}\text{HTO}$ surface, even though x is significantly increased to 20 mol%.

In comparison to the loaded copper materials, the R-space of the r- $\text{Cu}_{(4)}@\text{HTO}$ presents both the Cu-O contribution at 1.5 Å for the first shell and the Cu-Cu contribution at 2.2 Å (no phase correction) for the second shell, respectively, despite of the resemblance of the XANES spectra between r- $\text{Cu}_{(4)}@\text{HTO}$ and r- $\text{Cu}_{(5)}\text{HTO}$ as shown in Fig. S3d-f. As a result, the copper metal nanoparticles could form on the HTO surface during the thermal reduction under hydrogen, while the same copper precursor was introduced through impregnation instead of coprecipitation during the material preparation. The formation of copper metal nanoparticles on the r- $\text{Cu}_{(4)}@\text{HTO}$ surface is also in good agreement with the analysis of HAADF-STEM micrograph, as presented in some sporadic bright agglomeration in Fig. S3b and S3c. Above all, it concludes that our coprecipitation method can successfully facilitate the synthesis of the atomically dispersed HTO supported copper materials up to 20 mol% Cu loading within the structure. Furthermore, the selective hydrogenation for the valorization of biomass-derived platform chemicals is comprehensively studied as follows.

3.2. Catalytic activity

Scheme S1 illustrates the plausible reaction pathways and the relevant chemicals for catalytic hydrogenation/hydrogenolysis of HMF [9, 54]. Herein, catalytic hydrogenation of HMF to BHMF using the copper-derivatized HTO materials was studied, and the catalytic ratio of copper species to HMF is presumably 10 mol%. In general, the catalyst materials (10 mg) were placed along with HMF (0.08 mmol) and IPA (4 mL) in a glass liner, which was further transferred to the multi-vessel Biotage system. The catalytic hydrogenation of HMF was carried out at 125 °C under 5 bar pressure of H_2 for 1 h, and the conversion of HMF and the product yields after the reaction were analyzed by GC-FID. Fig. 4a presents that r- $\text{Cu}_{(5)}\text{HTO}$ can completely hydrogenate HMF and selectively transform HMF into BHMF with a nearly 100% yield. As the copper loading increases, the r- $\text{Cu}_{(10)}\text{HTO}$ exhibits comparable catalytic performance, concomitant with minor production of BHMTHF due to the over-hydrogenation. In comparison to the low reactivity for as-synthesized $\text{Cu}_{(5)}\text{HT}$ and calcined $\text{Cu}_{(5)}\text{HTO}$ catalysts, it infers that the copper species on the r- $\text{Cu}_{(5)}\text{HTO}$ surface become catalytically active for selective hydrogenation of HMF to BHMF after the thermal reduction under hydrogen. It could be attributed to the formation of atomically dispersed copper species with mixed valences, as previously discussed. In addition, low catalytic activity for HMF hydrogenation is observed using r- $\text{Cu}_{(4)}@\text{HTO}$ catalyst in which copper metal nanoparticles are otherwise conspicuously present after the thermal reduction.

To understand the reaction dynamics by using the r- $\text{Cu}_{(5)}\text{HTO}$ catalyst for hydrogenation of HMF to BHMF, we have investigated the effects of solvents, temperatures, hydrogen pressures as well as the recycling study. Fig. 4b presents the catalytic performance at 125 °C under 5 bar of H_2 for 1 h in different solvents. The results indicate that the aprotic solvent, acetone, hardly promotes BHMF formation, albeit the depletion of HMF. It could be attributed to the formation of condensed products through the aldol condensation between HMF and acetone catalyzed by the surface basicity of HTO derived materials, as previously reported [55]. On the contrary, the protic solvents, 2-propanol (IPA), and ethanol

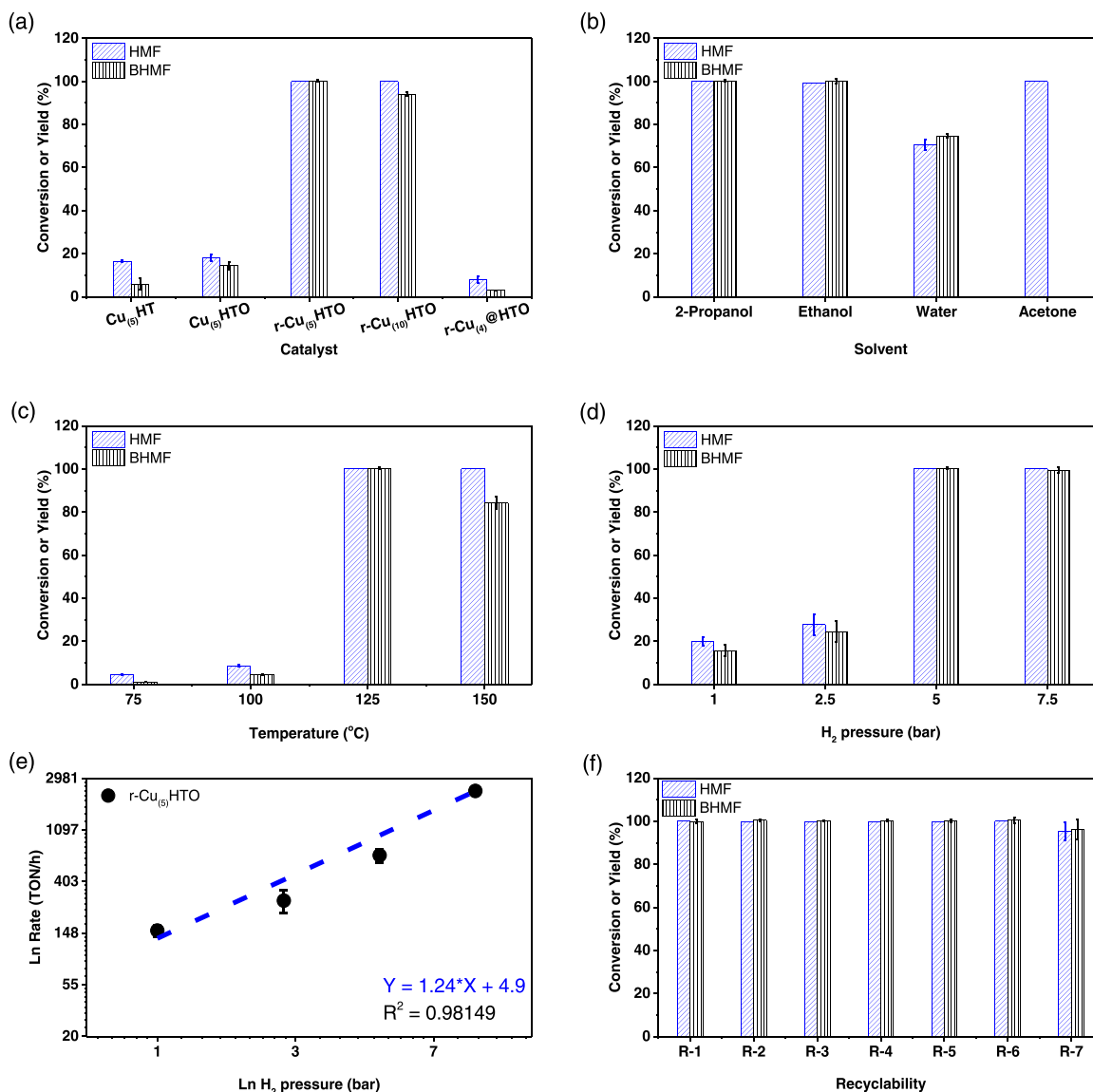


Fig. 4. (a) HMF conversion and BHMF yield over different catalysts in IPA under 5 bar of H₂ at 125 °C for 1 h, (b) effect of different solvents, (c) effect of temperature, (d) effect of H₂ pressure, (e) the reaction order of H₂ pressure, and (f) the recyclability study.

can serve as consummate solvents for the complete transformation of HMF to BHMF. However, a lower reactivity in water is observed. It could be attributed to the structural restoration of HTO to HT derived from the memory effect in an aqueous solution, which would lead to the dynamic change on the HTO surface for catalytic hydrogenation [56]. On the other hand, IPA is one well-known liquid-phase hydrogen resource for catalytic transfer hydrogenation (CTH), which can avoid the use of pressurized hydrogen gas. Therefore, the reaction task under the same condition with the pressurized N₂ up to 20 bar exhibits minor reactivity in 20.3% yield of BHMF with 12.5% HMF conversion, as shown in Fig. S8. This result infers that r-Cu₍₅₎HTO is not efficiently reactive for CTH reaction, and it could be due to the nature of derivatized metal oxide supports as previously reported [57]. Thus, the protic solvents such as IPA and ethanol are better hydrogen mediators for hydrogen gas in the catalytic hydrogenation of HMF [5,8,9].

Fig. 4c illustrates the effect of reaction temperatures, and the catalytic hydrogenation reaction was performed in IPA under 5 bar of H₂ for 1 h at temperatures ranging from 75 °C to 150 °C. The results indicate that the r-Cu₍₅₎HTO is unable to catalyze the hydrogenation of HMF to BHMF effectively at temperatures below 100 °C. However, as the reaction temperature increases to 125 °C, a substantial enhancement readily

reflects on the > 99% BHMF production yield with the 100% HMF conversion. While the reaction is carried out at 150 °C, BHMF yield drops evidently, concomitant with the coproduction of BHMTF, MFA, and DMF derived from hydrogenolysis and over-hydrogenation. Hence, the r-Cu₍₅₎HTO might direct the hydrogenation to the hydrogenolysis or over-hydrogenation of HMF at higher reaction temperatures.

The effects of hydrogen pressure were studied through the reaction performed at 125 °C in IPA for 1 h under the pressurized hydrogen ranging from 1 bar to 7.5 bar, as shown in Fig. 4d. The reactivity below 5 bar of hydrogen gas exhibits similarly compared to the one without hydrogen gas, as previously mentioned. As the hydrogen pressure elevates to 5 bar, the reactivity is significantly enhanced with a 100% HMF conversion and > 99% BHMF yield. The reactivity remains comparable while the hydrogen gas increases to 7.5 bar. No BHMTF but a negligible amount of 5-MF is observed. In addition, as depicted in Fig. 4e, the reaction order in respect of H₂ pressure was evaluated by analyzing the log-log plot of the conversion rate as a function of H₂ pressure. The slope representing the reaction order of H₂ pressure for HMF hydrogenation over r-Cu₍₅₎HTO is estimated as + 1.24. The positive value indicates that the H₂ pressure significantly influences the reaction rate, and the dissociation mechanism of hydrogen species is involved in the rate-

determining step, as previously reported [58]. The reaction order of almost +1 also suggests that the hydrogen molecule is heterolytically dissociated into a proton (H^+) and hydride (H^-) on the catalyst surface. Thus, the hydride species are active in hydrogenating HMF to BHMF [58,59]. Moreover, the positively charged copper sites can electronically interact with the carbonyl group via lone-pair electron of oxygen then activate the $C=O$ bond on HMF as previously suggested [6]. In this study, r-Cu₍₅₎HTO catalyst possessing the atomically dispersed copper species can foster the heterolytically-dissociated H_2 molecules for the selective hydrogenation of the carbonyl group of HMF, as shown in Scheme 1.

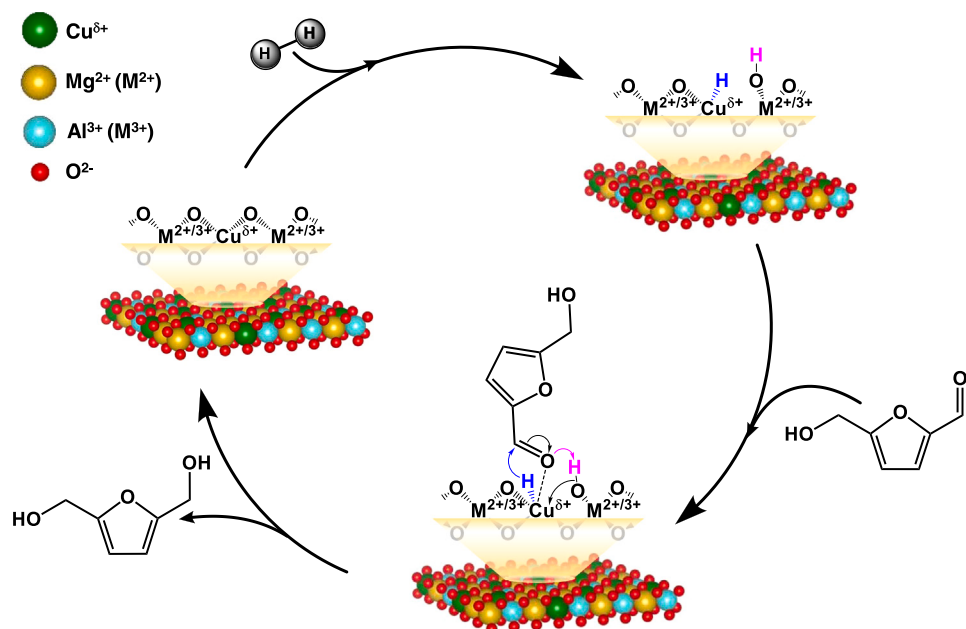
The apparent activation energy (E_a) for the selective hydrogenation of carbonyl groups to alcohol of biomass-derived furanics varied upon the substrate as well as the catalytic system [5,14]. The low E_a of 12.8 KJ.mol⁻¹ for furfural to furfural alcohol catalyzed by the hydroxide-supported Pt-based catalyst was recently reported [14], while the E_a of 74.07 KJ.mol⁻¹ for HMF to BHMF catalyzed by the copper-iron oxides bimetallic nanocatalyst was also reported lately [5]. As shown in Fig. S9a, the E_a of HMF catalyzed by r-Cu₍₅₎HTO was measured and estimated as 79.8 KJ.mol⁻¹ based on the Arrhenius equation while the HMF reaction was performed under low conversion at selected reaction temperatures. To understand the kinetics of the reaction, the catalytic tasks catalyzed by r-Cu₍₅₎HTO and r-Cu₍₁₀₎HTO were demonstrated and limited below 30% conversion under kinetically controlled condition. The catalytic performance was carried out under the same condition, except that HMF concentration was adjusted to 12.5-fold (1 mmol) higher than the regular one. The results reveal that r-Cu₍₅₎HTO can yield 11.9% BHMF with 13.3% HMF conversion, while r-Cu₍₁₀₎HTO can yield 28.3% BHMF with 29.9% HMF conversion, as shown in Fig. S9b. More active copper sites which are accounted for the enhancement of selective hydrogenation of HMF to BHMF are evidently present on r-Cu₍₁₀₎HTO surface, and the active copper sites remain homogeneously distributed on HTO while the copper loading increases in 2-fold quantity. It strongly corroborates the formation of atomically dispersed copper sites over the HTO surface as well as the structure-performance correlation.

Recyclability was studied using the spent catalyst after regeneration. The regeneration of the spent catalyst was performed by IPA washing with a sequential thermal reduction. As shown in Fig. 4f, the catalytic conversion of hydrogenation for HMF and the yield for BHMF remain comparably unaffected after repeating seven runs. To understand the

structural stability of the r-Cu₍₅₎HTO after reaction, the PXRD diffraction patterns of the regenerated spent samples were analyzed, and the results are identical to the fresh one, as presented in Fig. S10. The absence of Cu or CuO aggregates also supports that the consecutive thermal regeneration will not influence the degree of the atomically dispersed copper within the HTO structure. On the other hand, the elemental analysis for the spent samples after three subsequent runs was quantitatively determined by ICP-OES, as summarized in Table S4. The results reveal no significant decrease for the spent samples, and it concludes that there is no copper leaching from the r-Cu₍₅₎HTO during repetitive reactions. In addition, the absence of the traceable copper species in the filtrate by ICP-OES after the reaction, as listed in Table S5 complements the stability study. Therefore, the r-Cu₍₅₎HTO catalyst exhibits excellent recyclability and stability for the selective hydrogenation of HMF to produce BHMF.

4. Conclusion

In summary, we have successfully demonstrated that the atomically dispersed hydroxide-supported copper catalysts (Cu_(x)HTO) can be synthesized by the facile coprecipitation of metal precursors in methanolic solution under a controlled pH. The structural details of Cu₍₅₎HTO were comprehensively elucidated by a series of surface characterizations which evidently shared the presence of the mononuclearity of copper species over the hydroxide oxide. Moreover, the degree of copper dispersion remained hardly affected at least in a degree of 97% even though the molar amount of doping copper was elevated to 20% for Cu₍₂₀₎HTO. On the other hand, the r-Cu₍₅₎HTO was employed as the catalyst for HMF hydrogenation to BHMF under milder conditions than those previously reported. Optimally, it could completely hydrogenate HMF to BHMF with a 99% yield in IPA solvent at 125 °C under 5 bar of hydrogen for 1 h with stable recyclability. The reactivity study under different hydrogen pressures also revealed the hydrogen order greater than 1, which indicated that heterolytic dissociation of hydrogen molecules occurred on the surface of r-Cu₍₅₎HTO. On the contrary, the copper-loaded HTO (r-Cu₍₄₎@HTO) presented a poor catalytic performance in HMF hydrogenation under the same condition. Hence, the dramatic enhancement of HMF hydrogenation catalyzed by r-Cu₍₅₎HTO can be attributed to the high degree of copper dispersion which are situated homogeneously over the HTO surface as well as chemically



Scheme 1. The proposed mechanism for HMF hydrogenation to BHMF over the r-Cu₍₅₎HTO catalyst.

reactive for the carbonyl group (C=O).

CRediT authorship contribution statement

Raju Kumar: Conceptualization, Methodology, Investigation, Writing – original draft, Writing – review & editing and Visualization. **Hsin-Hui Lee:** Investigation. **En Chen:** Investigation. **Yuan-Peng Du:** Investigation, Writing – review & editing. **Chan-Yi Lin:** Investigation. **Warot Prasanseang:** Investigation. **Thanasak Solos:** Investigation. **Kittisak Choojun:** Investigation, Resources, Writing – review & editing. **Tawan Sooknoin:** Investigation, Resources, Writing – review & editing. **Rui-Kun Xie:** Investigation, Resources. **Jyh-Fu Lee:** Investigation, Resources, Writing – review & editing. **Po-Wen Chung:** Conceptualization, Methodology, Investigation, Resources, Writing – review & editing, Supervision, Project administration, Funding acquisition.

Declaration of Competing Interest

The authors declare that they have no known competing financial interests or personal relationships that could have appeared to influence the work reported in this paper.

Data availability

No data was used for the research described in the article.

Acknowledgements

We acknowledge the Advanced Materials Characterization lab, IAMS, Academia Sinica for the technical support in HR-TEM measurements, and Ms. Tsai-Yun Lee (The Instrumentation Centre at NTHU) for her support in measuring the ICP-OES. We also acknowledge the beamline TLS-17C1 of Taiwan Light Source in the National Synchrotron Radiation Research Center (NSRRC) for XAS study.

Budget

This work was supported by the National Science and Technology Council in Taiwan (111–2113-M-001–015) and the Academia Sinica in Taiwan (AS-iMATE-112-24).

Appendix A. Supporting information

Supplementary data associated with this article can be found in the online version at [doi:10.1016/j.apcatb.2023.122547](https://doi.org/10.1016/j.apcatb.2023.122547).

References

- [1] G. McCormack, Glasgow COP-26 Japan and Australia Weigh their Energy Options, ASIA-PACIFIC JOURNAL-JAPAN Focus. 19 (2021) 5661. <https://apjjf.org/2021/24/McCormack.html>.
- [2] K. Huang, X. Peng, L. Kong, W. Wu, Y. Chen, C.T. Maravelias, Greenhouse gas emission mitigation potential of chemicals produced from biomass, ACS Sustain. Chem. Eng. 9 (2021) 14480–14487, <https://doi.org/10.1021/acssuschemeng.1c04836>.
- [3] J.J. Bozell, G.R. Petersen, Technology development for the production of biobased products from biorefinery carbohydrates—the US Department of Energy's "Top 10" revisited, Green. Chem. 12 (2010) 539–554, <https://doi.org/10.1039/b922014c>.
- [4] J. Long, W. Zhao, Y. Xu, H. Li, S. Yang, Carbonate-catalyzed room-temperature selective reduction of biomass-derived 5-hydroxymethylfurfural into 2,5-bis(hydroxymethyl)furan, Catalysts 8 (2018) 633, <https://doi.org/10.3390/catal8120633>.
- [5] I. Elsayed, M.A. Jackson, E.B. Hassan, Hydrogen-free catalytic reduction of biomass-derived 5-hydroxymethylfurfural into 2,5-bis(hydroxymethyl)furan using copper–iron oxides bimetallic nanocatalyst, ACS Sustain. Chem. Eng. 8 (2020) 1774–1785, <https://doi.org/10.1021/acssuschemeng.9b05575>.
- [6] K.T.V. Rao, Y. Hu, Z. Yuan, Y. Zhang, C.C. Xu, Green synthesis of heterogeneous copper–alumina catalyst for selective hydrogenation of pure and biomass-derived 5-hydroxymethylfurfural to 2,5-bis(hydroxymethyl)furan, Appl. Catal. A Gen. 609 (2021), 117892, <https://doi.org/10.1016/j.apcata.2020.117892>.
- [7] J. Ohyama, A. Esaki, Y. Yamamoto, S. Arai, A. Satsuma, Selective hydrogenation of 2-hydroxymethyl-5-furfural to 2,5-bis(hydroxymethyl)furan over gold sub-nano clusters, RSC Adv. 3 (2013) 1033–1036, <https://doi.org/10.1039/C2RA22190J>.
- [8] K. Vikanova, E. Redina, G. Kapustin, M. Chernova, O. Tkachenko, V. Nissenbaum, L. Kustov, Advanced room-temperature synthesis of 2,5-bis(hydroxymethyl)furan—a monomer for biopolymers—from 5-hydroxymethylfurfural, ACS Sustain. Chem. Eng. 9 (2021) 1161–1171, <https://doi.org/10.1021/acssuschemeng.0c06560>.
- [9] T.-W. Tzeng, C.-Y. Lin, C.-W. Pao, J.-L. Chen, R.J.G. Nuguid, P.-W. Chung, Understanding catalytic hydrogenolysis of 5-hydroxymethylfurfural (HMF) to 2,5-dimethylfuran (DMF) using carbon-supported Ru catalysts, Fuel Process. Technol. 199 (2020), 106225, <https://doi.org/10.1016/j.fuproc.2019.106225>.
- [10] R. Šivec, M. Grilc, M. Huš, B. Likozar, Multicatalytic modeling of (hemi)cellulose hydrolysis and cascade hydrotreatment of 5-hydroxymethylfurfural, furfural, and levulinic acid, Ind. Eng. Chem. Res. 58 (2019) 16018–16032, <https://doi.org/10.1021/acs.iecr.9b00898>.
- [11] L. Hu, J. Xu, S. Zhou, A. He, X. Tang, L. Lin, J. Xu, Y. Zhao, Catalytic advances in the production and application of biomass-derived 2,5-dihydroxymethylfuran, ACS Catal. 8 (2018) 2959–2980, <https://doi.org/10.1021/acscatal.7b03530>.
- [12] S. Goswami, S. Dey, S. Jana, Design and synthesis of a unique ditopic macrocyclic fluorescent receptor containing furan ring as a spacer for the recognition of dicarboxylic acids, Tetrahedron 64 (2008) 6358–6363, <https://doi.org/10.1016/j.tet.2008.04.086>.
- [13] T. Pasini, G. Solinas, V. Zanotti, S. Albonetti, F. Cavani, A. Vaccari, A. Mazzanti, S. Ranieri, R. Mazzoni, Substrate and product role in the Shvo's catalyzed selective hydrogenation of the platform bio-based chemical 5-hydroxymethylfurfural, Dalt. Trans. 43 (2014) 10224–10234, <https://doi.org/10.1039/C4DT00304G>.
- [14] G. Gao, J. Remón, Z. Jiang, L. Yao, C. Hu, Selective hydrogenation of furfural to furfuryl alcohol in water under mild conditions over a hydrotalcite-derived Pt-based catalyst, Appl. Catal. B Environ. 309 (2022), 121260, <https://doi.org/10.1016/j.apcatb.2022.121260>.
- [15] N. Vinod, S. Dutta, Energy densification of biomass-derived furfurals to furanic biofuels by catalytic hydrogenation and hydrodeoxygenation reactions, Sustain. Chem. 2 (2021) 521–549, <https://doi.org/10.3390/suschem2030029>.
- [16] B. Pomeroy, M. Grilc, S. Gyergyek, B. Likozar, Catalyst structure-based hydroxymethylfurfural (HMF) hydrogenation mechanisms, activity and selectivity over Ni, Chem. Eng. J. 412 (2021), 127553, <https://doi.org/10.1016/j.cej.2020.127553>.
- [17] B. Pomeroy, M. Grilc, B. Likozar, Process condition-based tuneable selective catalysis of hydroxymethylfurfural (HMF) hydrogenation reactions to aromatic, saturated cyclic and linear poly-functional alcohols over Ni–Ce/Al 2 O 3, Green. Chem. 23 (2021) 7996–8002, <https://doi.org/10.1039/D1GC02086B>.
- [18] S. Sitthisa, T. Sooknoin, Y. Ma, P.B. Balbuena, D.E. Resasco, Kinetics and mechanism of hydrogenation of furfural on Cu/SiO2 catalysts, J. Catal. 277 (2011) 1–13, <https://doi.org/10.1016/j.jcat.2010.10.005>.
- [19] J. Feng, Y. He, Y. Liu, Y. Du, D. Li, Supported catalysts based on layered double hydroxides for catalytic oxidation and hydrogenation: general functionality and promising application prospects, Chem. Soc. Rev. 44 (2015) 5291–5319, <https://doi.org/10.1039/C5CS00268K>.
- [20] A.J. Kumalaputri, G. Bottari, P.M. Erne, H.J. Heeres, K. Barta, Tunable and selective conversion of 5-HMF to 2,5-furandimethanol and 2,5-dimethylfuran over copper-doped porous metal oxides, ChemSusChem 7 (2014) 2266–2275, <https://doi.org/10.1002/cssc.201402095>.
- [21] Q. Wang, J. Feng, L. Zheng, B. Wang, R. Bi, Y. He, H. Liu, D. Li, Interfacial structure-determined reaction pathway and selectivity for 5-(hydroxymethyl)furan hydrogenation over Cu-based catalysts, ACS Catal. 10 (2020) 1353–1365, <https://doi.org/10.1021/acscatal.9b03630>.
- [22] H. Niu, J. Luo, C. Li, B. Wang, C. Liang, Transfer hydrogenation of biomass-derived furfural to 2-methylfuran over Cu/ZnAl catalysts, Ind. Eng. Chem. Res. 58 (2019) 6298–6308, <https://doi.org/10.1021/acs.iecr.9b00408>.
- [23] P. Nagaiha, P. Gidyonu, M. Ashokraju, M.V. Rao, P. Challa, D.R. Burri, S.R. R. Kamaraju, Magnesium aluminate supported Cu catalyst for selective transfer hydrogenation of biomass derived furfural to furfuryl alcohol with formic acid as hydrogen donor, ChemistrySelect 4 (2019) 145–151, <https://doi.org/10.1002/slct.201803645>.
- [24] M.M. Villaverde, T.F. Garetto, A.J. Marchi, Liquid-phase transfer hydrogenation of furfural to furfuryl alcohol on Cu–Mg–Al catalysts, Catal. Commun. 58 (2015) 6–10, <https://doi.org/10.1016/j.catcom.2014.08.021>.
- [25] M. Flytzani-Stephanopoulos, B.C. Gates, Atomically dispersed supported metal catalysts, Annu. Rev. Chem. Biomol. Eng. 3 (2012) 545–574, <https://doi.org/10.1146/annurev-chembioeng-062011-080939>.
- [26] B.C. Gates, M. Flytzani-Stephanopoulos, D.A. Dixon, A. Katz, Atomically dispersed supported metal catalysts: perspectives and suggestions for future research, Catal. Sci. Technol. 7 (2017) 4259–4275, <https://doi.org/10.1039/C7CY00881C>.
- [27] J. Liu, Catalysis by supported single metal atoms, ACS Catal. 7 (2017) 34–59, <https://doi.org/10.1021/acscatal.6b01534>.
- [28] J.M. Thomas, R. Raja, D.W. Lewis, Single-site heterogeneous catalysts, Angew. Chem. Int. Ed. 44 (2005) 6456–6482, <https://doi.org/10.1002/anie.200462473>.
- [29] J. Fan, Y. Chen, X. Chen, Z. Wu, W. Teng, W. Zhang, Atomically dispersed iron enables high-efficiency electrocatalytic conversion of nitrate to dinitrogen on a N-coordinated mesoporous carbon architecture, Appl. Catal. B Environ. 320 (2023), 121983, <https://doi.org/10.1016/j.apcatb.2022.121983>.
- [30] F. Meng, M. Peng, Y. Chen, X. Cai, F. Huang, L. Yang, X. Liu, T. Li, X. Wen, N. Wang, D. Xiao, H. Jiang, L. Xia, H. Liu, D. Ma, Defect-rich graphene stabilized atomically dispersed Cu3 clusters with enhanced oxidase-like activity for

- antibacterial applications, *Appl. Catal. B Environ.* 301 (2022), 120826, <https://doi.org/10.1016/j.apcatb.2021.120826>.
- [31] C. Cometto, A. Ugoletti, E. Grazietti, A. Moretto, G. Bottaro, L. Armelao, C. Di Valentin, L. Calvillo, G. Granozzi, Copper single-atoms embedded in 2D graphitic carbon nitride for the CO₂ reduction, *Npj 2D Mater. Appl.* 5 (2021) 63, <https://doi.org/10.1038/s41699-021-00243-y>.
- [32] T. Guo, N. Tang, F. Lin, Q. Shang, S. Chen, H. Qi, X. Pan, C. Wu, G. Xu, J. Zhang, D. Xu, Y. Cong, High-loading single-atom copper catalyst supported on coordinatively unsaturated Al 2 O 3 for selective synthesis of homoallylboronates, *ChemSusChem* 13 (2020) 3115–3121, <https://doi.org/10.1002/cssc.202000536>.
- [33] Z. Yang, B. Chen, W. Chen, Y. Qu, F. Zhou, C. Zhao, Q. Xu, Q. Zhang, X. Duan, Y. Wu, Directly transforming copper (I) oxide bulk into isolated single-atom copper sites catalyst through gas-transport approach, *Nat. Commun.* 2019 10(1), 10 (2019) 1–7. <https://doi.org/10.1038/s41467-019-11796-4>.
- [34] S. Xie, W. Tan, Y. Li, L. Ma, S.N. Ehrlich, J. Deng, P. Xu, F. Gao, L. Dong, F. Liu, Copper Single Atom-Triggered Niobia-Ceria Catalyst for Efficient Low-Temperature Reduction of Nitrogen Oxides, *ACS Catal.* 12 (2022) 2441–2453, <https://doi.org/10.1021/acscatal.1c05661>.
- [35] G.V. Sagar, P.V.R. Rao, C.S. Srikanth, K.V.R.R. Chary, Dispersion and reactivity of copper catalysts supported on Al 2 O 3 –ZrO₂, *J. Phys. Chem. B* 110 (2006) 13881–13888, <https://doi.org/10.1021/jp0575153>.
- [36] B. Ravel, M. Newville, ATHENA, ARTEMIS, HEPHAESTUS: data analysis X-ray absorption spectroscopy using IFEFFIT, *J. Synchrotron Radiat.* 12 (2005) 537–541.
- [37] M. Yabushita, N. Shibayama, K. Nakajima, A. Fukuoka, Selective glucose-to-fructose isomerization in ethanol catalyzed by hydrotalcites, *ACS Catal.* 9 (2019) 2101–2109, <https://doi.org/10.1021/acscatal.8b05145>.
- [38] G. Hincapíe, D. López, A. Moreno, Infrared analysis of methanol adsorption on mixed oxides derived from Mg/Al hydrotalcite catalysts for transesterification reactions, *Catal. Today* 302 (2018) 277–285, <https://doi.org/10.1016/j.cattod.2017.05.052>.
- [39] C. Mebrahtu, F. Krebs, S. Perathoner, S. Abate, G. Centi, R. Palkovits, Hydrotalcite based Ni-Fe/(Mg, Al)O x catalysts for CO 2 methanation – tailoring Fe content for improved CO dissociation, basicity, and particle size, *Catal. Sci. Technol.* 8 (2018) 1016–1027, <https://doi.org/10.1039/C7CY02099F>.
- [40] I.S.P. Campisano, C.B. Rodella, Z.S.B. Sousa, C.A. Henriques, V. Teixeira da Silva, Influence of thermal treatment conditions on the characteristics of Cu-based metal oxides derived from hydrotalcite-like compounds and their performance in bio-ethanol dehydrogenation to acetaldehyde, *Catal. Today* 306 (2018) 111–120, <https://doi.org/10.1016/j.cattod.2017.03.017>.
- [41] R. Djebek, M. Motak, T. Grzybek, M. Galvez, P. Da Costa, A short review on the catalytic activity of hydrotalcite-derived materials for dry reforming of methane, *Catalysts* 7 (2017) 32, <https://doi.org/10.3390/catal7010032>.
- [42] K.J.D. MacKenzie, R.H. Meinhold, B.L. Sherriff, Z. Xu, 27Al and 25Mg solid-state magic-angle spinning nuclear magnetic resonance study of hydrotalcite and its thermal decomposition sequence, *J. Mater. Chem. 3* (1993) 1263–1269, <https://doi.org/10.1039/jm9930301263>.
- [43] Z. Sun, A. Couto Vasconcelos, G. Bottari, M.C.A. Stuart, G. Bonura, C. Cannilla, F. Frusteri, K. Barta, Efficient catalytic conversion of ethanol to 1-butanol via the guerbet reaction over copper and nickel-doped porous, *ACS Sustain. Chem. Eng.* 5 (2017) 1738–1746, <https://doi.org/10.1021/acsuschemeng.6b02494>.
- [44] K.A. Cychoz, R. Guillet-Nicolas, J. García-Martínez, M. Thommes, Recent advances in the textural characterization of hierarchically structured nanoporous materials, *Chem. Soc. Rev.* 46 (2017) 389–414, <https://doi.org/10.1039/C6CS00391E>.
- [45] W.E. Taifan, Y. Li, J.P. Baltrus, L. Zhang, A.I. Frenkel, J. Baltrusaitis, Operando Structure Determination of Cu and Zn on Supported MgO/SiO₂ Catalysts during Ethanol Conversion to 1,3-Butadiene, *ACS Catal.* 9 (2019) 269–285, <https://doi.org/10.1021/acscatal.8b03515>.
- [46] M.-F. Luo, Y.-J. Zhong, X.-X. Yuan, X.-M. Zheng, TPR and TPD studies of CuOCeO₂ catalysts for low temperature CO oxidation, *Appl. Catal. A Gen.* 162 (1997) 121–131, [https://doi.org/10.1016/S0926-860X\(97\)00089-6](https://doi.org/10.1016/S0926-860X(97)00089-6).
- [47] Z. Gao, C. Li, G. Fan, L. Yang, F. Li, Nitrogen-doped carbon-decorated copper catalyst for highly efficient transfer hydrogenolysis of 5-hydroxymethylfurfural to convertibly produce 2,5-dimethylfuran or 2,5-dimethyltetrahydrofuran, *Appl. Catal. B Environ.* 226 (2018) 523–533, <https://doi.org/10.1016/j.apcatb.2018.01.006>.
- [48] N. Marcella, J.S. Lim, A.M. Plonka, G. Yan, C.J. Owen, J.E.S. van der Hoeven, A. C. Foucher, H.T. Ngan, S.B. Torrisi, N.S. Marinkovic, E.A. Stach, J.F. Weaver, J. Aizenberg, P. Sautet, B. Kozinsky, A.I. Frenkel, Decoding reactive structures in dilute alloy catalysts, *Nat. Commun.* 13 (2022) 832, <https://doi.org/10.1038/s41467-022-28366-w>.
- [49] C. Angelici, F. Meirer, A.M.J. van der Eerden, H.L. Schaink, A. Goryachev, J. P. Hofmann, E.J.M. Hensen, B.M. Weckhuysen, P.C.A. Bruijnincx, Ex Situ and Operando Studies on the Role of Copper in Cu-Promoted SiO₂ –MgO Catalysts for the Lebedev Ethanol-to-Butadiene Process, *ACS Catal.* 5 (2015) 6005–6015, <https://doi.org/10.1021/acscatal.5b00755>.
- [50] Y. Chen, W. Liu, P. Yin, M. Ju, J. Wang, W. Yang, Y. Yang, C. Shen, Synergistic effect between Ni single atoms and acid–base sites: Mechanism investigation into catalytic transfer hydrogenation reaction, *J. Catal.* 393 (2021) 1–10, <https://doi.org/10.1016/j.jcat.2020.11.019>.
- [51] J. Jiang, C. Tu, C. Chen, Y. Lin, Highly Selective Silica-supported Copper Catalysts Derived from Copper Phyllosilicates in the Hydrogenation of Adipic Acid to 1,6-hexanediol, *ChemCatChem* 10 (2018) 5449–5458, <https://doi.org/10.1002/cctc.201801580>.
- [52] K. Asakura, Y. Iwasawa, A structure model as the origin of catalytic properties of metal-doped MgO systems, *Mater. Chem. Phys.* 18 (1988) 499–512, [https://doi.org/10.1016/0254-0584\(88\)90019-3](https://doi.org/10.1016/0254-0584(88)90019-3).
- [53] Y. Qu, Z. Li, W. Chen, Y. Lin, T. Yuan, Z. Yang, C. Zhao, J. Wang, C. Zhao, X. Wang, F. Zhou, Z. Zhuang, Y. Wu, Y. Li, Direct transformation of bulk copper into copper single sites via emitting and trapping of atoms, *Nat. Catal.* 1 (2018) 781–786, <https://doi.org/10.1038/s41929-018-0146-x>.
- [54] X. Wang, C. Zhang, B. Jin, X. Liang, Q. Wang, Z. Zhao, Q. Li, Pt–Carbon interaction-determined reaction pathway and selectivity for hydrogenation of 5-hydroxymethylfurfural over carbon supported Pt catalysts, *Catal. Sci. Technol.* 11 (2021) 1298–1310, <https://doi.org/10.1039/D0CY01920H>.
- [55] K. Pupovac, R. Palkovits, Cu/MgAl 2 O 4 as Bifunctional Catalyst for Aldol Condensation of 5-Hydroxymethylfurfural and Selective Transfer Hydrogenation, *ChemSusChem* 6 (2013) 2103–2110, <https://doi.org/10.1002/cssc.201300414>.
- [56] T. Baskaran, J. Christopher, A. Sakthivel, Progress on layered hydrotalcite (HT) materials as potential support and catalytic materials, *RSC Adv.* 5 (2015) 98853–98875, <https://doi.org/10.1039/CSRA19909C>.
- [57] W. Fang, A. Riisager, Recent advances in heterogeneous catalytic transfer hydrogenation/hydrogenolysis for valorization of biomass-derived furanic compounds, *Green. Chem.* 23 (2021) 670–688, <https://doi.org/10.1039/D0GC03931D>.
- [58] Y. Takeda, M. Tamura, Y. Nakagawa, K. Okumura, K. Tomishige, Characterization of Re–Pd/SiO₂ catalysts for hydrogenation of stearic acid, *ACS Catal.* 5 (2015) 7034–7047, <https://doi.org/10.1021/acscatal.5b01054>.
- [59] K. Tomishige, Y. Nakagawa, M. Tamura, Selective hydrogenolysis and hydrogenation using metal catalysts directly modified with metal oxide species, *Green. Chem.* 19 (2017) 2876–2924, <https://doi.org/10.1039/C7GC00620A>.